Supporting Information for

Elevator mechanism dynamics in a sodium-coupled dicarboxylate transporter.

Colin D. Kinz-Thompson,[1,†] Maria Louisa Lopez-Redondo,[2,‡] Christopher Mulligan,[3] David B. Sauer,[2,§] Jennifer J. Marden,[2] Jinmei Song,[2] Emad Tajkhorshid,[4] John F. Hunt,[5] David L. Stokes,[2] Joseph A. Mindell,[6*] Da-Neng Wang,[2*] Ruben L. Gonzalez, Jr.[1*]

*****Corresponding Authors: Ruben, L. Gonzalez, Jr. (rlg2118@columbia.edu), Da-Neng Wang (da-neng.wang@med.nyu.edu), Joseph A. Mindell (mindellj@ninds.nih.gov).

Supporting Information Text

1. Global, variational Bayes hidden Markov modeling (vbHMM).

Global vbHMMs as implemented in the tMAVEN software package (1) were estimated in a manner similar to a previously described single trajectory vbHMM implemented in the software package vbFRET (2). vbFRET is a Bayesian inference-based 'maximum evidence' method (3), which allowed one to determine the simplest HMM that sufficiently accounts for the complexity of the smFRET data (2, 4, 5). In this method, one can find the most parsimonious HMM for smFRET data by estimating several HMMs, each with an increasing number of hidden states, then calculating the 'evidence' for each HMM and choosing the one with the maximum evidence value (2). As seen in the directed acyclic graph (Fig. S5), the only difference between vbFRET, and the global vbHMM used here is that an ensemble of E_{FRET} versus time trajectories is assumed to be independent and identically distributed (I.I.D.) from the same HMM parameters in the global vbHMM model. Thus, all data points then contribute to the expectation and maximization equations for the hyperparameters governing the posterior probability distribution, as opposed to only those from a single trajectory as is done for vbFRET. This is equivalent to considering one large, concatenated trajectory with vbFRET, where however there is no conditional dependence for the hidden state on the previous hidden state for neighboring data points from different trajectories. Instead, the first data point of each trajectory depends on the initial-state probability distribution denoted here by π. As can be done with vbFRET, model selection can be performed by calculating the evidence lower bound (ELBO) for each model and choosing that model with the largest value.

To demonstrate the efficacy of using model selection with global vbHMMs, we simulated multiple four-state time series, performed model selection, and compared this to an autocorrelation function (ACF) analysis (Fig. S7). The two-point autocorrelation function (6) of a stationary stochastic process or signal, y(t), describes how similar the process remains after some time lag, τ, and can be calculated as

$$ACF(\tau) \equiv \langle \delta y(0) \cdot \delta y(\tau) \rangle = \int_{-\infty}^{\infty} \int_{-\infty}^{\infty} d\delta y(0) \cdot d\delta y(t) \cdot y(0) \cdot y(\tau) \cdot P(\delta y(0), \delta y(\tau))$$

where $\delta y(\tau) = y(\tau) - \langle y \rangle$, angular brackets denote an expectation value, P(x) is the probability distribution function of x, and

$$P\big(\delta y(0), \delta y(\tau)\big) = P\big(\delta y(\tau) | \delta y(0)\big) \cdot P\big(\delta y(0)\big).$$

For a discrete, zero-mean signal, A(t), composed of N data points, the ACF can be estimated as

$$ACF(\tau) \equiv \langle A(0) A(\tau) \rangle = \lim_{N \to \infty} \frac{1}{N} \sum_{i=1}^{N} A_i A_{i+\tau}$$

Thus, assuming normally distributed values of $A_i A_{i+\tau}$, the ACF and the associated precision is distributed as a student-T distribution, $T_\nu(x|\mu, \sigma^2)$ with ν degrees of freedom, as $T_{N-1}(ACF(\tau)|\bar{x}, (\sum_i (x_i - \bar{x})^2)/(N(N-1)))$, where $x_i = A_i A_{i+\tau}$, and $\bar{x} = \frac{1}{N} \sum_i A_i A_{i+\tau}$. This is derived from the posterior marginal of a normal-distribution likelihood with a normal-gamma prior with κ=0, α=−1/2, and β=0 (7). The same formulas can be used to calculate an ACF from multiple signal trajectories that are independent and identically distributed; for instance the ACF at time τ would then include terms $A_i^0 A_{i+\tau}^0 + A_i^1 A_{i+\tau}^1 + \cdots + A_i^M A_{i+\tau}^M$, where the superscript denotes an index over *M* number of signal trajectories. We refer to this as the ensemble ACF.

For some specific types of signals, we can calculate an analytical form of the ACF for comparison to observed ACFs. First, if a time-dependent signal was stationary at zero and distributed according to $y(t) \sim \mathcal{N}(0, \sigma^2)$, where $\mathcal{N}$ denotes a normal distribution, and σ^2 is the variance, the $ACF(t) = \sigma^2 \cdot \delta(t)$, where $\delta(t)$ is a Dirac delta function, which is one when t=0, and zero otherwise. Second, consider a zero-mean Markov chain with N states that are normally distributed according to $\mathcal{N}(\mu_i, \sigma_i^2)$ for the ith state, but where $\langle y \rangle = 0$. Also, consider that the rate constant for the transition from the ith state to the jth state, k_{ij}, can be written as a rate constant matrix, K, with the associated Q matrix (K but where the on-diagonals are the negative sum of the rate constants out the ith state). Notably, a vector of the probability of being in a particular state, P(t), given an initial probability vector, P(0), can then be written $P(t) = e^{Qt} \cdot P(0)$, where *e* denotes a matrix-exponential. If the Markov chain is in state i, the signal value at a particular time can be written $y(t) \sim \mu_i + N_i$, where $N_i \sim \mathcal{N}(0, \sigma_i^2)$. Thus, the ACF for this model is

$$\langle y(0)y(t) \rangle = \sum_i \sum_j \int_{N_i} \int_{N_j} (\mu_i + N_i)(\mu_j + N_j) \cdot P(j, t; i, 0; N_t; N_0),$$

where

$$P(j, t; i, 0; N_t; N_0) = P(j, t|i, 0) \cdot P_i(t = \infty) \cdot \mathcal{N}(0, \sigma_j^2) \cdot \mathcal{N}(0, \sigma_i^2).$$

Therefore

$$\begin{aligned}\langle y(0)y(t) \rangle &= \sum_{i,j} \mu_i \mu_j \cdot d_j \cdot e^{Qt} \cdot d_i \cdot P_i(t = \infty) + \sum_i \sigma_i^2 \cdot P_i(t = \infty) \cdot \delta(t) \\ &\equiv ACF_{MC}(t) + \langle \sigma^2 \rangle \cdot \delta(t),\end{aligned}$$

where d_i is a vector with a 1 in position i, and ACF_{MC} is the contribution from the Markov chain. Additionally, we note that $P(j, t|i, 0) \cdot P(i) = d_j \cdot e^{Qt} \cdot d_i \cdot P_i(t = \infty)$ can be rewritten with a spectral expansion as $\sum_i C_i e^{-\lambda_i t}$, where C_i is a weighting factor, and λ_i is an eigenvalue of e^{Qt}. Thus, for this Markov chain model with normally distributed noise, the ACF can be written as a weighted sum of *N* exponential decays with a term at t=0 corresponding to the average amount of uncorrelated, normally distributed noise. Therefore, for this model, the difference between ACF(t=0) and the next data point ACF(t=dt) is mostly $\langle \sigma^2 \rangle$, and the rest of the ACF is described by various exponential decays to zero.

In order to simulate single-molecule trajectories, we used the stochastic simulation algorithm (8) with the parameters in Table S1 with additive, normally distributed noise. From these 400 trajectories, we estimated global HMMs with one through six states as described above. As expected, the HMM with four states had the largest ELBO (Fig. S7). Additionally, we calculated the ACFs of these HMMs as described above. Notably, of these ACFs, only those for HMMs with four or more states are sufficient to match the individual and ensemble ACFs of the simulated trajectories (Fig. S7). Thus, the most parsimonious global HMM determined by this method also recapitulates the kinetic results of a model-free ACF method, but has the additional benefit as a model-based method of providing a mechanistic interpretation of those results.

2. Photobleaching detection.

We detect photobleaching by using shape-based Bayesian model selection to choose the photobleaching time, or lack thereof, in a fluorescence intensity trajectory (9). Each model, M_T, that we choose between is similar in that before some time, T, the data points are assumed to be distributed according to a normal distribution with some mean, μ_1, and some precision, λ_1 (i.e., inverse variance $\lambda=\sigma^{-2}$), which we do not care about, while the data points after time T are distributed according to a normal distribution with mean of zero, and some different precision, λ_2. We then calculate the probability of each M_T, having marginalized out the means and precisions so that the conclusions are relevant regardless of those values, and then use Bayesian inference to select the M_T that gives the best estimate of the photobleaching time as is supported by the available data. Practically, this method assigns all observed fluorescence at the beginning of a trajectory into the same 'on' state, usually with a large variance to account for different intensity states that compose the 'on' state, and then finds the last point where the data can be described as dropping to zero. For an ensemble of intensity trajectories, we perform model selection twice. The first time, we use uniform priors for the photobleaching time, while the second time, we use the independently calculated photobleaching times to infer an ensemble photobleaching rate constant, and then repeat the photobleaching time model selection calculation using this photobleaching rate constant to define the prior probability distribution for T for all of the independent intensity trajectories.

Mathematically, the likelihood for one of these models M_T is

$$P(\{x\}|\mu_1,\lambda_1,\lambda_2,T)=\prod_{t<T}\mathcal{N}(x_t|\mu_1,\lambda_1^{-1})\prod_{t\geq T}\mathcal{N}(x_t|0,\lambda_2^{-1}),$$

where $\mathcal{N}(x|\mu,\sigma^2)$ is a normal distribution with mean μ, and variance σ^2. Using a prior probability distribution of

$$\begin{aligned}P(\mu_1,\lambda_1,\lambda_2)&=NG(\mu_1,\lambda_1|\alpha_1,\beta_1,\kappa_1,m_1)\cdot G(\lambda_2|\alpha_2,\beta_2)\\&=\left[(2\pi)^{-\frac{1}{2}}(\kappa_1\lambda_1)^{\frac{1}{2}}e^{-\frac{\kappa_1\lambda_1}{2}(\mu_1-m_1)^2}\cdot\beta_1^{\alpha_1}\Gamma(\alpha_1)^{-1}\lambda_1^{\alpha_1-1}\,e^{-\beta_1\lambda_1}\right]\cdot\left[\beta_2^{\alpha_2}\Gamma(\alpha_2)^{-1}\lambda_2^{\alpha_2-1}\,e^{-\beta_2\lambda_2}\right],\end{aligned}$$

where NG is a joint normal-gamma distribution, and G is a gamma distribution,(7) we obtain a posterior probability distribution of the same form but with updated hyperparameters (denoted by primes)

$$P(\mu_1,\lambda_1,\lambda_2|\{x\},T)=NG(\mu_1,\lambda_1|\alpha_1',\beta_1',\kappa_1',m_1')\cdot G(\lambda_2|\alpha_2',\beta_2'),$$

where

$$\begin{aligned}\alpha_1'&=\alpha_1+T/2\\\beta_1'&=\beta_1+\frac{1}{2}\sum_{i=0}^{T}(x_i-\langle x\rangle)^2+\frac{\kappa_1T(\langle x\rangle-m_1)^2}{2(\kappa_1+T)}\\\kappa_1'&=\kappa_1+T\\m_1'&=\frac{\kappa_1m_1+T\langle x\rangle}{\kappa_1+T}\\\alpha_2'&=\alpha_2+(N-T)/2\\\beta_2'&=\beta_2+\frac{1}{2}\sum_{i=T}^{N}x_i^2\,,\end{aligned}$$

where N is the total number of data points. However, we do not particularly care about the exact values of μ_1, λ_1, or λ_2, so instead, we can marginalize them out to find the probability that of the observed data given the model M_T (i.e., the "evidence"), regardless of these nuisance parameters. In this case, we find

$$\begin{aligned} P(\{x\}|M_T) &= P(\{x\}_{t<T}|M_T) \cdot P(\{x\}_{t\geq T}|M_T) \\ &= \left[\frac{\Gamma(\alpha'_1)}{\Gamma(\alpha_1)} \cdot \frac{\beta_1^{\alpha_1}}{\beta_1'^{\alpha'_1}} \cdot \left(\frac{\kappa_1}{\kappa'_1}\right)^{\frac{1}{2}} \cdot (2\pi)^{-\frac{T}{2}}\right] \cdot \left[\frac{\Gamma(\alpha'_2)}{\Gamma(\alpha_2)} \cdot \frac{\beta_2^{\alpha_2}}{\beta_2'^{\alpha'_2}} \cdot (2\pi)^{-\frac{(N-T)}{2}}\right]. \end{aligned}$$

Now, with the evidence for the data given a photobleaching time, $P(\{x\}|M_T)$, we use Bayesian inference to select best photobleaching model (i.e., the model best supported by the data, regardless of the individual parameters) as the largest value of

$$P(M_T|\{x\}) = \frac{P(\{x\}|M_T) \cdot P(M_T)}{\sum_{T=0}^{N} P(\{x\}|M_T) \cdot P(M_T)}.$$

As discussed above, $P(M_T)$ is at first taken to be a constant and all trajectories are analyzed independently. Then, we infer the ensemble photobleaching rate constant using Bayesian inference with an exponential distribution as a likelihood, and a gamma distribution as the conjugate prior, and therefore also the posterior. As a result, we estimate $k_{PB} = (1+n)/(1+\sum_{i=0}^{n} T_i)$, where *i* indexes the different trajectories. Then, we use an exponential distribution as the prior $P(M_T) = k_{PB}e^{-k_{PB}T}$, where k_{PB} is treated as a deterministic value. Finally, we note that these model selection calculations are performed in log-space, and that we subtract the maximum of all the log terms (i.e., scale by a constant) from both the numerator and denominator in order the to avoid computer underflow.

Since the models used for model selection in this algorithm are not comprehensive in the sense that they do not account for every experimental nuance of the data, we believe it is best to manually examine the selected model and the underlying fluorescence intensity trajectory to ensure that they are reasonably well matched, and so that one can manually adjust the photobleaching time when they do not match due to unaccounted for experimental behaviors (*e.g.*, deviations from Gaussian emissions).

3. Calculation of Cycle Fluxes.

For the mechanistic scheme for transport in Fig. 5, the following terms are necessary to calculate cycle fluxes to be calculated. For shorter notation, we use $t \equiv k_t$, $d' \equiv k'_d$, $d'' = k''_d$,$A_o \equiv k'_a[A]_o^m$, $A_i \equiv k'_a[A]_i^m$, $B_o \equiv k''_a[B]_o^n$, and $B_i \equiv k''_a[B]_i^n$. The cycle flux for any cycle is

$$J_\kappa = J_{\kappa+} - J_{\kappa-} = (\Pi_{\kappa+} - \Pi_{\kappa-})\,\Sigma_\kappa/\Sigma,$$

where

$$\Pi_{a+} - \Pi_{a-} = t^2 d'(A_o - A_i),$$

$$\Pi_{b+} - \Pi_{b-} = t^2 d''(B_o - B_i),$$

$$\Pi_{c+} - \Pi_{c-} = t^2 d' d''(A_o B_o - A_i B_i),$$

$$\Sigma_a = 2td'' + d''^2,$$

$$\Sigma_b = t(A_o + A_i) + A_o A_i,$$

$$\Sigma_c = 1, \text{ and}$$

$$\begin{aligned}\Sigma = 2t^3[d''(4d' + 2A_i + A_o) + (2A_iB_i + A_oB_o + A_oB_i + B_oA_i)] \\ + 2t^2\big[d''^2(2d' + A_i + A_o) \\ + d''\big((2(A_o + A_i) + (B_o + B_i) + 2d')d' + (A_iB_i + B_oA_i + 2A_oA_i + A_oB_o + A_oB_i)\big) \\ + \big((A_oB_o + A_iB_i)d' + (A_oB_oA_i + A_oA_iB_i + A_oB_oB_i + B_oA_iB_i)\big)\big] \\ + 2t\big[d''^2\big((A_o + A_i)d' + A_oA_i + d'^2\big) + d''\big((A_oB_o + A_iB_i)d' + (A_oB_oA_i + A_oA_iB_i)\big) + (A_oB_oA_iB_i)\big].\end{aligned}$$

From these equations, the functional form of J_c for each first order rate constant, k, in Fig. 5 is $[ak + b + ck^{-1}]^{-1}$ where the coefficients *a*, *b*, and *c* depend on the other rate constants. This functional form has a maximum at $k = \sqrt{c/a}$, so there is an optimal value of k_t that maximizes transport cycle flux under for a given set of substrate concentrations. Finally, we note that Σ has 90 terms, and thus so does J_c. Due to the changes to the energy landscape in Fig. 6, 68 of the terms in J_c increase the magnitude of J_c, 18 decrease it, and 4 do not change it.

To find the optimal parameters to describe previously published succinate transport data, a target energy function of $\left(J^{expt} - (J_b + J_c)\right)^2$ was used for $J^{expt}([X] = K_M) = \frac{V_{max}}{2}$ and $J^{expt}([X] = 1000K_M) = V_{max}$ for the sodium titration in their Figure 3 ($K_M = 41.7\ mM$, and $V_{max} = 53.5\ nmol\ mg^{-1}min^{-1} = 58.3\ s^{-1}$), and the succinate titration in their Figure 6 ($K_M = 1.0\ \mu M$, and $V_{max} = 232.6\ nmol\ mg^{-1}min^{-1} = 253.4\ s^{-1}$) (10). The collective energy function for both experiments was minimized using an affine invariant MCMC ensemble sampler (11) with 200 walkers, a 1,000 step burn-in period, and a 10,000 step production period from which every 100th point was taken as a sample to avoid autocorrelation within the samples.

The steady-state probability of apo VcINDY in Buffer HX was calculated from the mechanism in Fig. 5 by setting $[B]_o = [B]_i = 0$, using the estimates for k'_a, $\langle k \rangle \equiv k_t$, and k'_d (Fig. S14) and $[A]_o = [A]_i = [Na^+] = 0.1M$, to calculate the steady state probability $P_{apo} = P_{C_o} + P_{C_i}$ as

$$P_{apo} = \frac{3\langle k\rangle^3 + k'_a[Na^+]^3\langle k\rangle^2}{3\langle k\rangle^3 + 4k'_a[Na^+]^3\langle k\rangle^2 + {k'_a}^2[Na^+]^6\langle k\rangle}.$$

4. X-ray Data Collection and Structure Determination.

Crystals were frozen in liquid nitrogen with the crystallization solution serving as the cryoprotectant. X-ray data were collected at the Advanced Photon Source Beamlines 19-ID and 19-BM. Data processing and scaling were performed using the HKL2000 software (12). All crystals were of space group $P2_1$ with unit cell dimensions around a = 106 Å, b = 102 Å, c = 171 Å, β = 99°, and contained four molecules per asymmetric unit. The structures were determined by molecular replacement using the structure of VcINDY (PDB: 5UL9) (13) with sodium and citrate removed as the initial search model, followed by repeated cycles of model building in Coot (14), and refinement in Phenix (Table S2) (15).

5. Analysis of Rate Constant Uncertainty for HMM-based Inference.

Rate constants inferred using HMMs have at least two-forms of uncertainty. The first is the equivalent of “fitting error,” in which the uncertainty in the value of an inferred rate constant decreases with increasing number of observations modeled by the HMM. The second is caused by molecular heterogeneity through non-uniform processes such as protein damage (*e.g.*, oxidation), post-translational modifications, and even slow degrees of freedom that are orthogonal to the observation or reaction coordinates (see Austin *et al.* (16)); most importantly, the amount of this heterogeneity is not typically known *a priori*. This section demonstrates that the "fitting error" type of uncertainty from an HMM is much less than that from molecular heterogeneity in a typical single-molecule study.

To begin, the uncertainty in HMM-derived rate constants and the associated transition-state activation energy barrier will be derived. Assuming single-molecule data is collected from a Markovian, two-state system,

$$A \underset{k_{-1}}{\overset{k_1}{\rightleftharpoons}} B,$$

when N sequential measurements are made, each with time period of τ, then the expected number of measurements where a single molecule is found in state A is

$$\langle N_A \rangle = \left(\frac{k_1}{k_1 + k_{-1}} \right) N.$$

In any one measurement period spent in state A, the probability of a transition occurring during that time period is the transition probability

$$P_{AB} = \int_0^\tau dt \cdot k e^{-k_1 t} = 1 - e^{-k_1 \tau},$$

and so, the expected number of transitions from state A to B is

$$\langle N_{AB} \rangle = (1 - e^{-k_1 \tau}) \langle N_A \rangle,$$

while the expected number of times a transition does not occur is

$$\langle N_{AA} \rangle = 1 - \langle N_{AB} \rangle = e^{-k_1 \tau} \langle N_A \rangle.$$

When using an HMM to model the kinetics of a single-molecule time series, the primary goal is to infer the "transition matrix" because this contains the kinetic information about the molecule. Because of the Markov property, each row of the transition matrix is a distinct model where a Dirichlet distribution is used to account for the splitting probabilities of remaining in (on-diagonal) or exiting from (off-diagonals) the state represented by the row. In the case of the two-state system above, for a single-molecule beginning in state A, the transition probability for remaining in state A (P_{AA}) or transitioning to state B (P_{AB}) is then modeled as

$$Dirichlet(\{P_{AA}, P_{AB}\} \mid \{\alpha_{AA}, \alpha_{AB}\})$$

where α is the Dirichlet concentration parameter. With a multinomial likelihood function for a transition occurring, which is the approach used for HMMs, the values of α that will be inferred by an HMM are

$$\alpha_{AA} = \langle N_{AA} \rangle + \alpha_{0,AA} \approx \langle N_{AA} \rangle$$

$$\alpha_{AB} = \langle N_{AB} \rangle + \alpha_{0,AB} \approx \langle N_{AB} \rangle$$

where the α_0 are prior hyperparameters that are small and can be ignored.

The transition probability obtained from a transition matrix is thus inferred from the (posterior) Dirichlet distribution as the expectation value $\mu_i = \frac{\alpha_i}{\sum_i \alpha_i} \equiv \frac{\alpha_i}{\alpha_0}$ and the variance of this estimate is $\sigma_i^2 = \frac{\alpha_i}{\alpha_0} \frac{(\alpha_0 - \alpha_i)}{\alpha_0} \frac{1}{(\alpha_0 + 1)}$. In the two-state case above, the HMM-based estimate for P_{AB} from N measurements is thus $\mu_{AB} \pm \sigma_{AB}$, where

$$\mu_{AB} = (1 - e^{-k_1 \tau}), \qquad \text{and}$$

$$\sigma_{AB} = \left[\frac{e^{-k_1\tau}(1-e^{-k_1\tau})}{\left(1+\frac{k_{-1}}{k_1+k_{-1}}N\right)}\right]^{1/2}.$$

A complementary expression is obtained for μ_{BA} by exchanging k_1 and k_{-1}.

A transition probability can be transformed into a rate constant by using the transformation $k(P) = -\frac{\ln(1-P)}{\tau}$, where k is a rate constant and P is its associated transition probability. The Jacobian for this transformation is

$$\left|\frac{dk(P)}{dP}\right| = \frac{1}{(1-P)\tau}.$$

Using this information to transform the estimate for the transition probability estimate $\mu_{AB} \pm \sigma_{AB}$ into an estimate for the rate constant $\tilde{\mu}_{AB} \pm \tilde{\sigma}_{AB}$, where the tilde denotes rate constant-space, the transition matrix-based estimate of the rate constant for the transition from state A to state B (*i.e.*, k_1) is $\tilde{\mu}_{AB} \pm \tilde{\sigma}_{AB}$, where

$$\tilde{\mu}_{AB} = k_1, \qquad \text{and}$$

$$\tilde{\sigma}_{AB} = \left[\frac{e^{+k_1\tau}-1}{\tau^2\left(1+\frac{k_{-1}}{k_1+k_{-1}}N\right)}\right]^{1/2}.$$

In an appropriately designed experiment with more than a handful of measurements (*i.e.*, $N \gg 1$ and $k_1\tau \ll 1$), the uncertainty simplifies to

$$\tilde{\sigma}_{AB} \approx \left[\frac{k_1(k_1+k_{-1})}{k_{-1}\tau N}\right]^{\frac{1}{2}},$$

which can be rearranged to find the number of measurements necessary to obtain a specific amount of uncertainty in k_{AB}, as

$$N(\tilde{\sigma}_{AB}) \approx \frac{k_1(k_1+k_{-1})}{k_{-1}\tau\,\tilde{\sigma}_{AB}^2}.$$

Furthermore, it is possible to transform the rate constant estimate to an estimate of the activation energy barrier. In the Arrhenius approach, rate constants are understood to arise from thermally activated barrier crossings. The barrier crossing process has an attempt frequency, A, and an activation energy barrier, E_a. The transformation of a rate constant into an Arrhenius-style activation barrier is

$$\mathrm{E_A}(k) = -k_B T \ln\frac{k}{A},$$

where the thermal energy is set by the Boltzmann constant, k_B, and the temperature, T. The Jacobian for this transformation is

$$\left|\frac{d\mathrm{E_A}(k)}{dk}\right| = \frac{k_B T}{k}.$$

Using this information to transform the estimate for the rate constant $\tilde{\mu}_{AB} \pm \tilde{\sigma}_{AB}$ into an estimate for the activation energy $\hat{\mu}_{AB} \pm \hat{\sigma}_{AB}$, where the hat denotes activation energy-space, we find that the transition matrix-based estimate of E_a for the transition from state A to state B is $\hat{\mu}_{AB} \pm \hat{\sigma}_{AB}$, where

$$\hat{\mu}_{AB} = -k_B T \ln\frac{k_1}{A}, \qquad \text{and}$$

$$\hat{\sigma}_{AB} = \left[\frac{e^{+k_1\tau} - 1}{\tau^2 \left(1 + \frac{k_{-1}}{k_1 + k_{-1}} N\right)} \right]^{1/2} .$$

In an appropriately designed experiment with more than a handful of measurements (*i.e.*, $N \gg 1$ and $k_1\tau \ll 1$), the uncertainty simplifies to

$$\hat{\sigma}_{AB} \approx k_B T \left[\frac{k_1 + k_{-1}}{k_1 k_{-1} \tau N}\right]^{1/2} ,$$

which can be inverted to find the number of measurements necessary to obtain a specific amount of uncertainty in the estimate of E_a for the transition from state A to state B as

$$N(\hat{\sigma}_{AB}) \approx \frac{k_B^2 T^2 (k_1 + k_{-1})}{k_1 k_{-1} \tau \, \hat{\sigma}_{AB}^2} .$$

This analysis of the uncertainty in the HMM-inferred activation energy barriers was applied to the global HMM models of the VcINDY E_{FRET} data sets in this study (Figs. S8 and S9) to understand the precision with which the HMMs describe the VcINDY substrate translocation reaction energy landscape. To do so, a two-state system was posited with forward and reverse rate constants taken as typical rate constants from the VcINDY HMMs in Fig. S9 of $k \equiv k_1 = k_{-1} = 0.4 \, s^{-1}$, and a measurement period taken as the EMCCD exposure time used in these experiments of $\tau = 0.025 \, s^{-1}$. Together these parameters yield a hypothetical experiment where $k\tau = 0.01$, which is significantly less than 1.0 and which is ten-fold less than the cutoff where HMMs begin to exhibit effects from missed events (17). The uncertainty in the HMM-inferred activation energy barriers for this hypothetical system, which was designed to approximate the kinetics of the VcINDY HMMs in this work, are shown in Fig. S11.

For the VcINDY data sets collected in this study, the precision in the inferred activation energies is approximately $\hat{\sigma} \approx 0.01$ kcal/mol (Fig. S11; green dashed lines). This is because each of these data sets is comprised of ~10^6 measurements, and this large number of measurements results in the HMM-inferred activation barriers being approximately 65-times more precise than the available thermal energy. Notably, the energy barrier that would be inferred from an analysis of a single E_{FRET} trajectory that was the average length before photobleaching is approximately twice as precise as the available thermal energy (Fig. S11; orange dashed lines). In the classic study where Frauenfelder and coworkers investigate dispersion in the activation energy of diatomic gas molecules dissociating from myoglobin, protein conformational dynamics was found to create approximately 1 kcal/mol of dispersion in the activation energy distribution (see Figs. 13 and 24 in Ref. 16) (16). Given the comparable number of degrees of freedom, it is likely that all proteins in the 10^4-10^5 Da range exhibit similar effects of conformational dynamics on the order of ~1 kcal/mol. Whether such heterogeneity is due to jumps between discrete conformational states or relatively slow diffusion over “rough” conformational landscapes, the average behavior observed across a mesoscopic ensemble from a single-molecule experiment may not accurately represent any one existing kinetic state, but instead be a reflection of the stochastic “irreproducibilities” of small mesoscopic ensembles (18). For instance, at room temperature, a 1 kcal/mol uncertainty in an activation energy (*e.g.*, due to molecular heterogeneity) would yield a 5-fold difference in a rate constant. Thus, given the extreme heterogeneity observed in the raw VcINDY smFRET data (Figs. 3, 4), the approximately two-fold differences in HMM-determined rate constants for VcINDY (Fig. S9) should be interpreted as being within the uncertainty of molecular heterogeneity.

6. Change-point modeling of E_{FRET} Trajectories

Transition density plots (TDPs) are two-dimensional histograms that reveal which E_{FRET} states are involved in a transition. On one axis of a TDP is the E_{FRET} value of the initial state prior to a transition occurring, and on the other axis is the E_{FRET} value of final state after the transition occurs. Thus, a TDP shows which E_{FRET} states are involved in the transitions observed from an ensemble of E_{FRET} trajectories. If the observed E_{FRET} states are not very heterogeneous and are specific to unique molecular states, then the E_{FRET} transitions that show up in a TDP can reveal insightful mechanistic information about the underlying biomolecular states. Importantly, the use of TDPs inherently invokes the Markov assumption by representing the dynamics of a time series in a reduced fashion depending only the instantaneous transition between the initial and final states. Additionally, constructing a TDP requires a model for emission, noise, and dynamics in order to identify where the transitions occur in an E_{FRET} trajectory in the first place. Consequently, these model-based requirements decrease the impact that TDPs have in revealing unique mechanistic information not already captured by the model. As such, change-point modeling has gained popularity as a minimal model-based approach with limited assumptions involved in detecting transitions in E_{FRET} time series (19, 20).

In this work, we utilized change-point modeling to detect transitions and construct TDPs of VcINDY E_{FRET} trajectories (Fig. S4). Transitions were detected in a single forward-pass by constructing a dwell in a putative state beginning at measurement point *i* and ending at point *j*; if no transition was detected, the length of the putative dwell is increased by one measurement period (*i.e.*, it then ends at measurement *j+1*) and the process repeats. If a transition to a new E_{FRET} state does occur, then by definition: (*i*) the dwell in the initial E_{FRET} state must truly end at measurement period *j*, and (*ii*) the E_{FRET} value of the next E_{FRET} state must be different than that of the first E_{FRET} state. With this in mind, the E_{FRET} value of the first E_{FRET} state in this putative dwell beginning at *i* and ending at *j* is then estimated by the average of the signal values, y_k, comprising that dwell as

$$\mu_1 = \frac{1}{j-i+1} \cdot \sum_{k=i}^{j} y_k.$$

Notably, this is the maximum-likelihood estimate for a Gaussian-distributed emission model, demonstrating how specifying an emission model is intrinsic to estimating the E_{FRET} state. A transition is then defined to occur if the jump in E_{FRET} values from this first E_{FRET} state to the second E_{FRET} state, $|\mu_2 - \mu_1|$ where μ_2 is the E_{FRET} value of the second E_{FRET} state, is greater than a cutoff threshold, Δ. Unfortunately, it is not known where the dwell in the second E_{FRET} state ends in a forward-pass, which makes it effectively impossible to estimate μ_2. To address this limitation, we instead take a local sampling of the post-dwell data to assess whether the subsequent data appears to be in one or more E_{FRET} states that are different than the first E_{FRET} state. To avoid the effects of sub-exposure time-averaging (*i.e.*, camera blurring) (21), we specify a time-lag period, *n*, and then estimate this post-dwell signal as

$$\mu_2 = \frac{1}{\sigma} \cdot \sum_{k=j+n}^{j+n+\sigma-1} y_k,$$

where σ is the sampling time. While other change-point detection algorithms use model-based probabilities to assess the likelihood of a transition between two states (19, 20), our approach instead detects transitions by identifying the end of a dwell, which occurs when the difference between the putative dwell versus the subsequent signal is greater than a pre-determined threshold (*i.e.*, if $|\mu_2 - \mu_1| > \Delta$) (Fig. S4A). Thus, our approach utilizes less restrictive modeling assumptions than others. Furthermore, the use of a time-lag avoids the complications of camera-blurring in transition detection. However, our approach does not remove camera-blurring from the resulting idealized trajectory, and instead yields short camera-blurred states of length less than or equal to n. To address this, we implement a post-processing step to eliminate these short dwells created by camera blurring by merging them into the previous or subsequent dwell time. If we consider three dwells in a row, each with average signal value μ_i, where $i \in (1,2,3)$, and $t_2 \leq n$ where t_i is the length of the dwell, then the middle dwell is merged into the first dwell if $|\mu_2 - \mu_1| < |\mu_3 - \mu_2|$, and is otherwise merged into the last dwell (Fig. S4B).

Overall, change-point modeling is a very effective method to detect transitions, and is implemented in the tMAVEN software v0.3.0 (1). Fig. S4C shows the change-point modeling results for a particularly dynamic E_{FRET} trajectory of VcINDY^{int} in buffer HS with $n = 1$ and $\sigma = 3$, which are the parameters we used to analyze all VcINDY E_{FRET} trajectories. In particular, filtering the data with the Chung-Kennedy filter (22) reveals the just how well the idealized trajectory matches the data. Using the transitions identified through change-point modeling, the initial E_{FRET} value for a transition occurring at time i and final E_{FRET} values occurring at time $i + \sigma$ from the raw E_{FRET} trajectories was used to create TDPs for all VcINDY E_{FRET} datasets (Fig. S5). To remove any instances of acceptor fluorophore photoblinking or photobleaching, all transitions involving an E_{FRET} state with a change-point modeling-based idealized E_{FRET} value less than 0.05 were excluded. Notably, these TDPs do not provide significant mechanistic clarity into the VcINDY E_{FRET} trajectories. There are no clearly isolatable E_{FRET} states, and the transitions occur over a very broad range of nearly all possible E_{FRET} values. However, these TDPs are consistent with the HMM-based modeling performed in the main text, as transitions occur primarily between neighboring states that are ~0.2-0.4 E_{FRET} values apart, which is consistent with the notion that the translocation motions are non-cooperative between the protomers of the VcINDY homodimer. Additionally, this behavior was independent of buffer and smFRET signal (Fig. S5), which is consistent with the minimal buffer dependence we observed in kinetics of the HMM-based modeling (Figs. S8-S9).

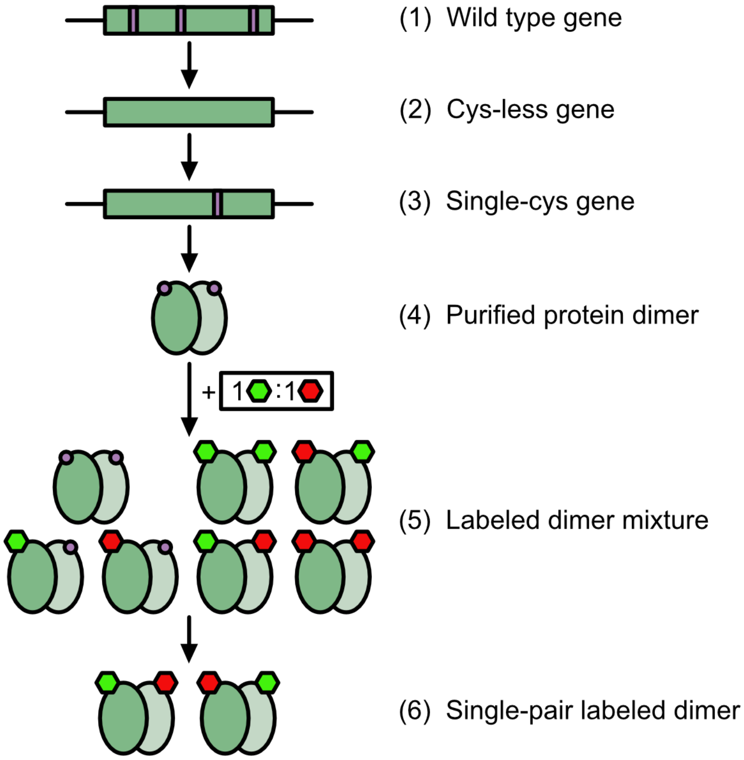

Fig. S1. Cartoon schematic of approach to yield donor- and acceptor- fluorophore-labeled VcINDY homodimers. Site-directed mutagenesis is used to remove all codons encoding cysteine from a plasmid-based "wild type" VcINDY gene (1) to yield a "cys-less" variant (2), and used further to introduce a single codon encoding cysteine (3). This is over-expressed in *Escherichia coli* (*E. coli*), and purified to yield homodimers with single-cysteine containing protomers (4). The homodimers are labeled with a 1:1 ratio of maleimide-conjugated donor- and acceptor-fluorophores (5). Only those homodimers labeled with both a single donor- and single acceptor-fluorophore are computationally selected after imaging (6).

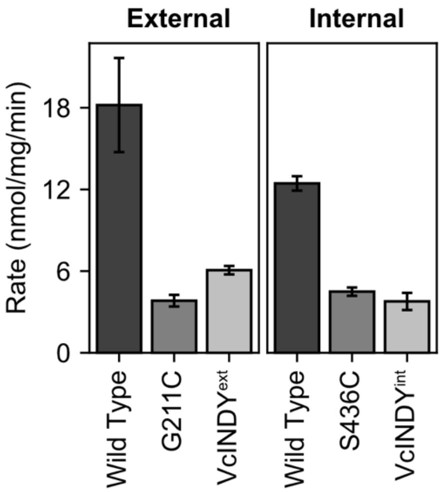

Fig. S2. VcINDY biochemical transport assays. Transport rates of proteoliposome-embedded VcINDY homodimers for the external (left) and internal (right) smFRET pair labeled positions. Wild type (i.e., cysteine-containing) assays were performed as control separately for each labeling position. Error bars are from triplicate technical replicates.

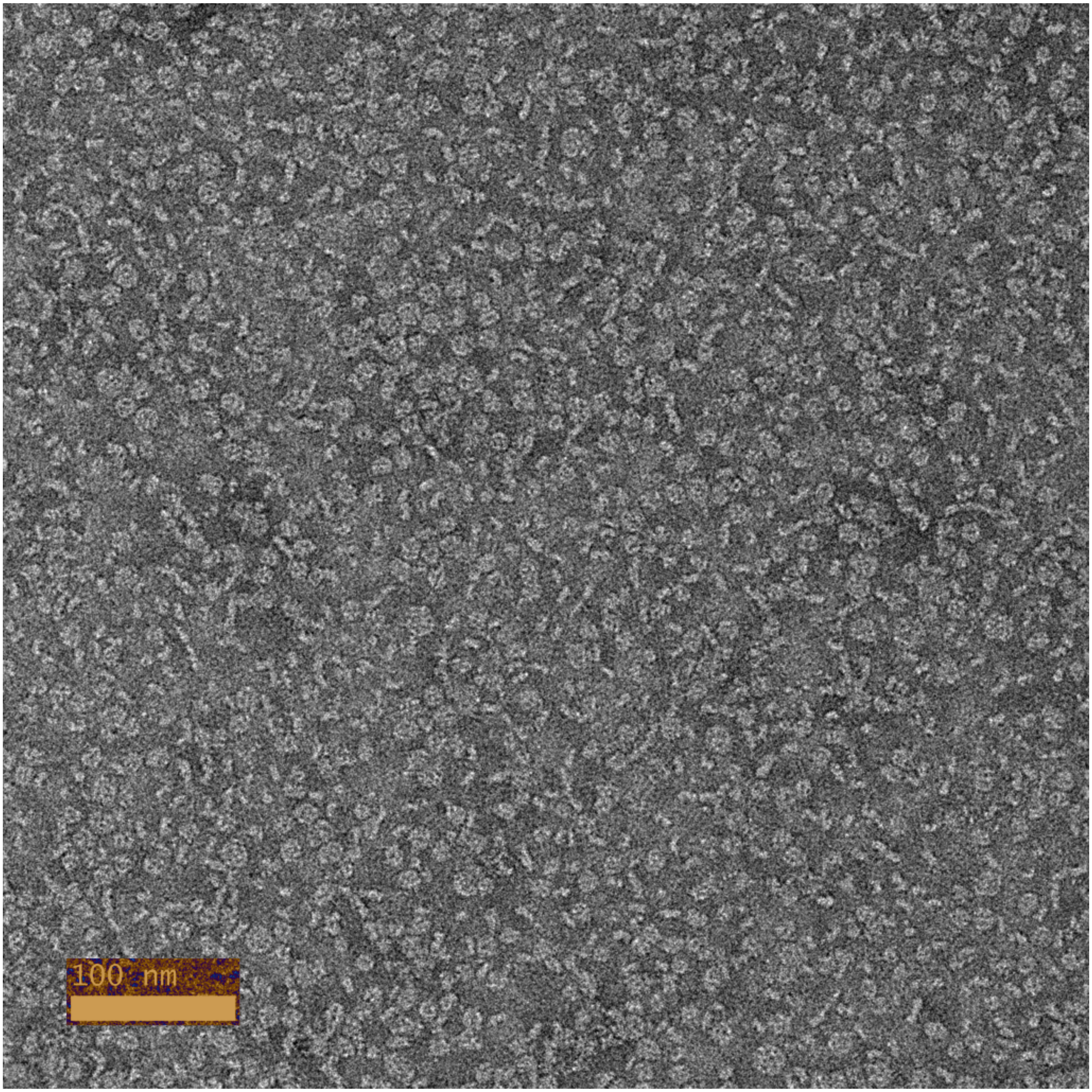

Fig. S3. Negative stain electron microscopy of VcINDY reconstituted into lipid nanodiscs. Both top and side views of nanodiscs were seen. The nanodiscs had a diameter of ~108 Å and each contained one VcINDY dimer. The sample was uniform and no aggregation was observed.

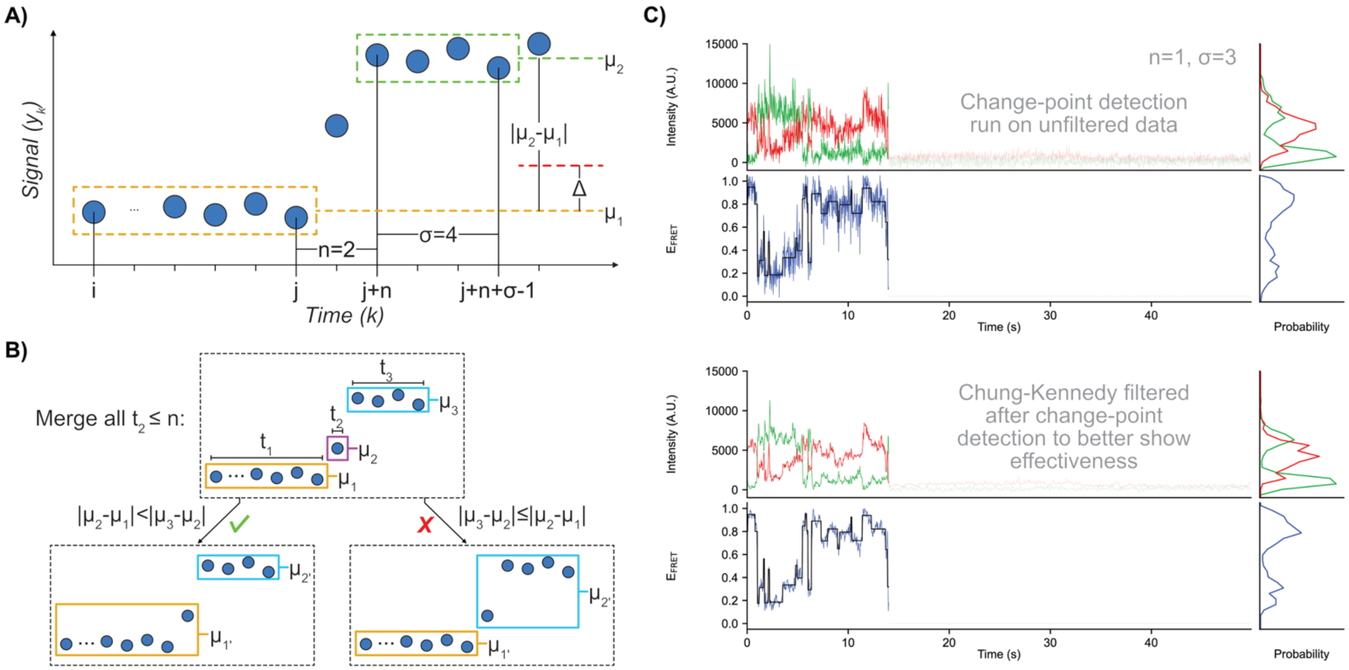

Fig. S4. Theory of change-point modeling. (A) Schematic diagram of a change-point being identified in a forward-pass when the difference in average signal values for a putative dwell (orange) and an estimate of an unknown future state (green) is greater than a threshold value, Δ. Measurements where a transition occurs during the integration period (e.g., camera blurring) are avoided by use of a time-lag period, *n*. (B) Schematic diagram depicting the merging of short-lived states which can appear due to signal blurring. The short-lived state is merged with the closest neighboring state, and the idealized signal value of that state is re-estimated. (C) Example of change-points detected with *n*=1 and σ=3 for a particularly dynamic VcINDY^{int} E_{FRET} trajectory (top). After change-point modeling, the idealized E_{FRET} trajectory (black) is left untouched, and the data were filtered with the Chung-Kennedy filter to better demonstrate the effectiveness of the change-point modeling (bottom).

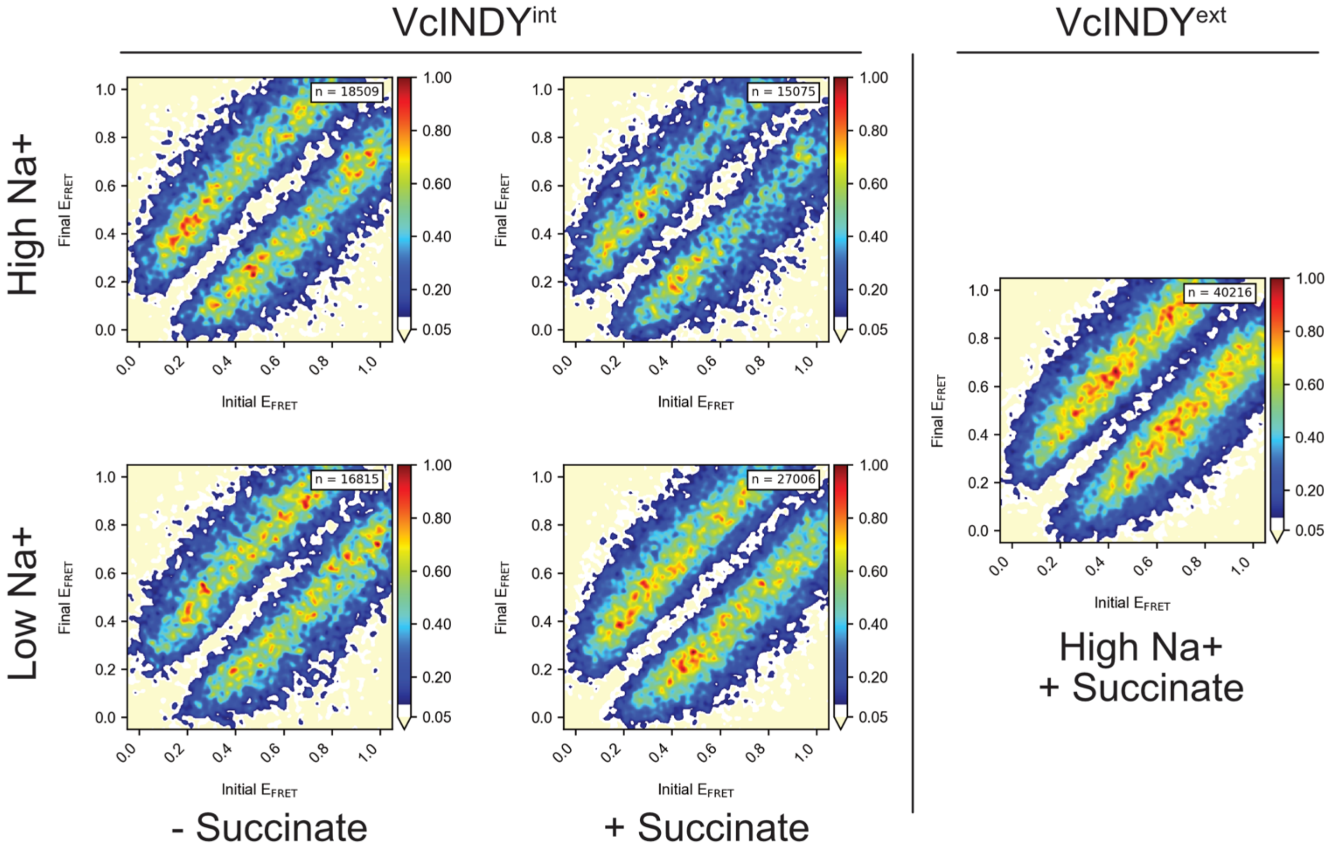

Fig. S5. Transition density plots of raw VcINDY E_{FRET} data. Transitions were detected using change-point modeling as described in Section 6. Legend value of *n* is the number of transitions in each dataset.

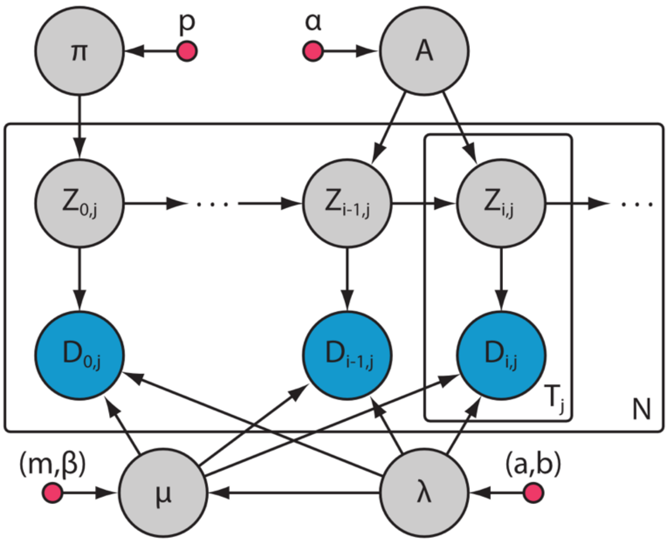

Fig. S6. Directed acyclic graph for a global, variational Bayes HMM. Pink nodes represent hyperparameters, grey nodes represent unobserved variables, and blue nodes represent observed variables. T_j is the number of data points in the jth trajectory, and $D_{i,j}$ corresponds to the ith data point of the jth trajectory. Arrows represent conditional dependencies.

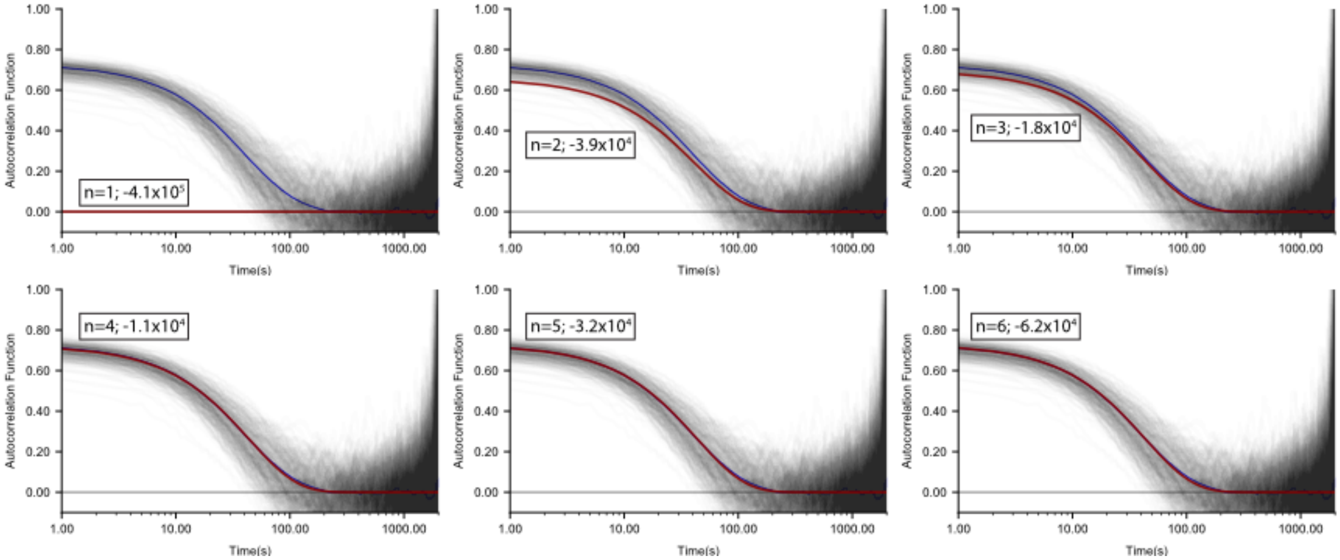

Fig. S7. Autocorrelation function analysis of global HMMs with various number of hidden states of simulated, four-state E_{FRET} trajectories. Individual ACFs (black), ensemble ACF (blue), and global HMM ACF (red). The maximum ELBO HMM (n=4; ln(ELBO)= $-1.1\text{x}10^4$) matches the number of E_{FRET} states in the simulation.

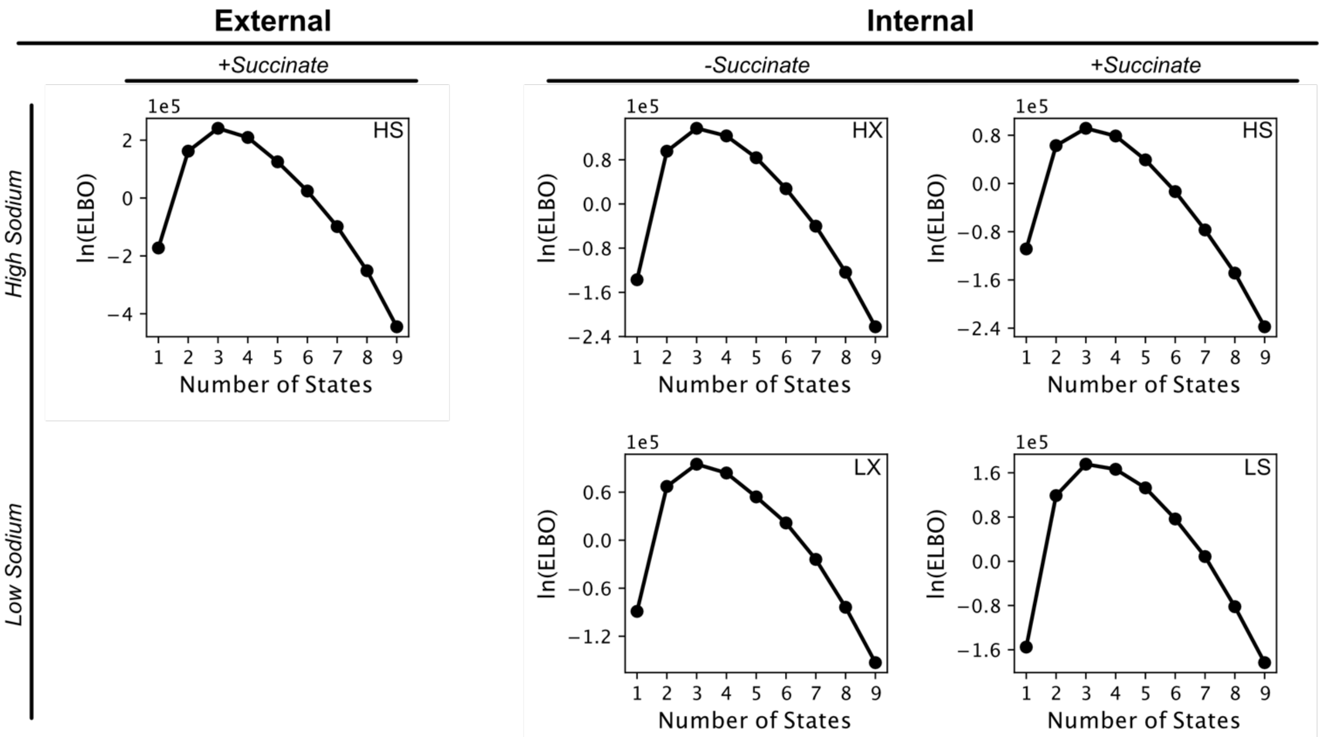

Fig. S8. Substrate dependence of evidence lower bound (ELBO) calculations for global HMMs of VcINDY smFRET experiments. The maximum ELBO model is the HMM that best represents the set of E_{FRET} trajectories for those substrate conditions.

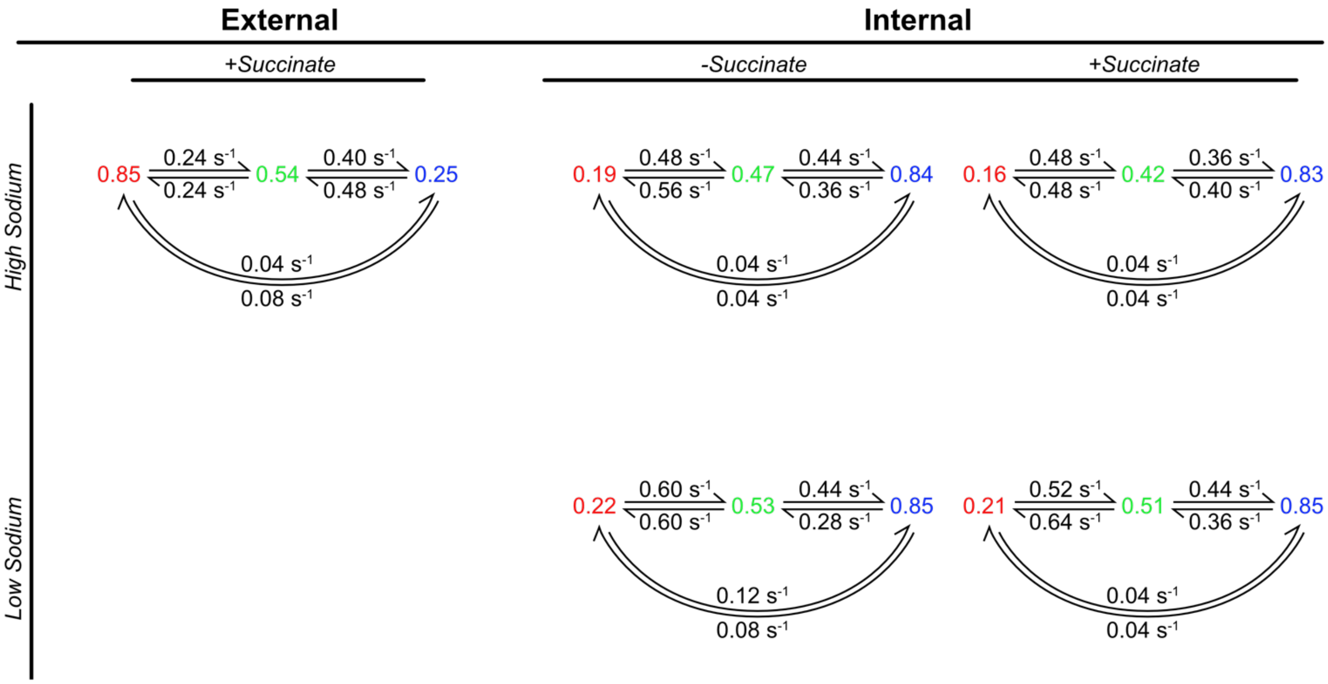

Fig. S9. Substrate dependence of the HMM with maximum ELBO for global HMMs of VcINDY smFRET experiments. For each kinetic scheme, states are denoted by the mean E_{FRET} value of that state, which was inferred from the HMM. Rate constants for transitions between states are shown above the arrows.

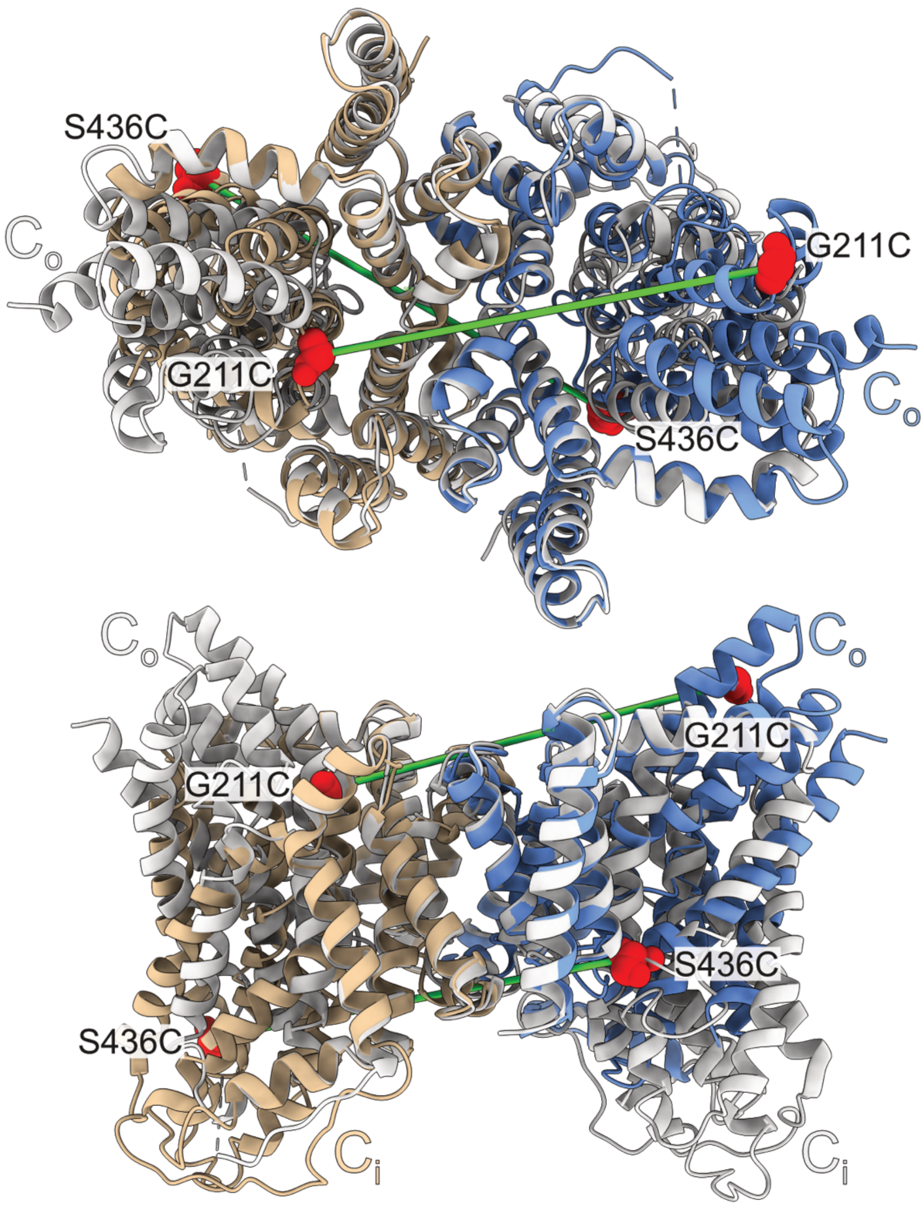

Fig. S10. Structural alignment of VcINDY showing labeling site distances in the C_i-C_o asymmetric conformation. Structures of the C_i-C_i (PDB ID 5ULE; tan) and C_o-C_o (PMDB ID PM0080216; blue) conformations were aligned by their scaffold domains. Protomers from these structures used in the alignment but not used in the C_i-C_o asymmetric conformation are shown in grey. Labeling site residues G211C and S436C are shown in red with green lines showing the ~50 Å and ~59 Å distances, respectively, between the labeling sites in an asymmetric mixed conformation. Views shown are from the exterior, looking down on the membrane (top) and from the side through the membrane (bottom).

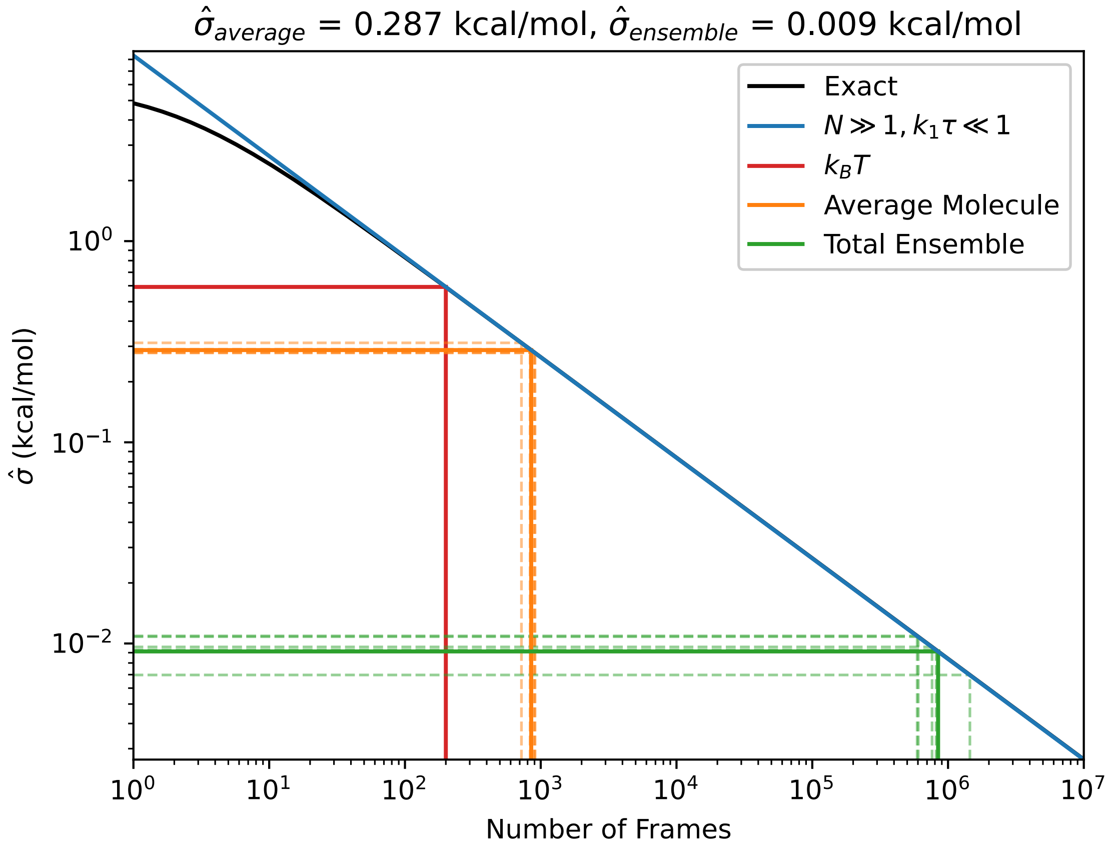

Fig. S11. Analysis of energy barrier inferred by an HMM. Plot of uncertainty in activation energy barrier in a two-state system modeled with an HMM as a function of increasing number of recorded measurement frames (black) with the approximation for a large number of frames (blue). Vertical and horizonal line pairs denote the achieved uncertainty given a number of frames for: thermal energy (red); the average length of an E_{FRET} time series before photobleaching in the data sets collected in this work (dashed orange), and the average across all data sets (solid orange); and the total length of all E_{FRET} time series before photobleaching in the data sets collected in this work (dashed green), and the average across all data sets (solid green). The uncertainty achieved for the green lines is comparable to that for the HMM-inferred rate constants in Fig. S9. To approximate the systems in Fig. S9, both forward and reverse rate constants were k = 0.4 s^{-1} and the measurement period was τ = 0.025 s in this calculation.

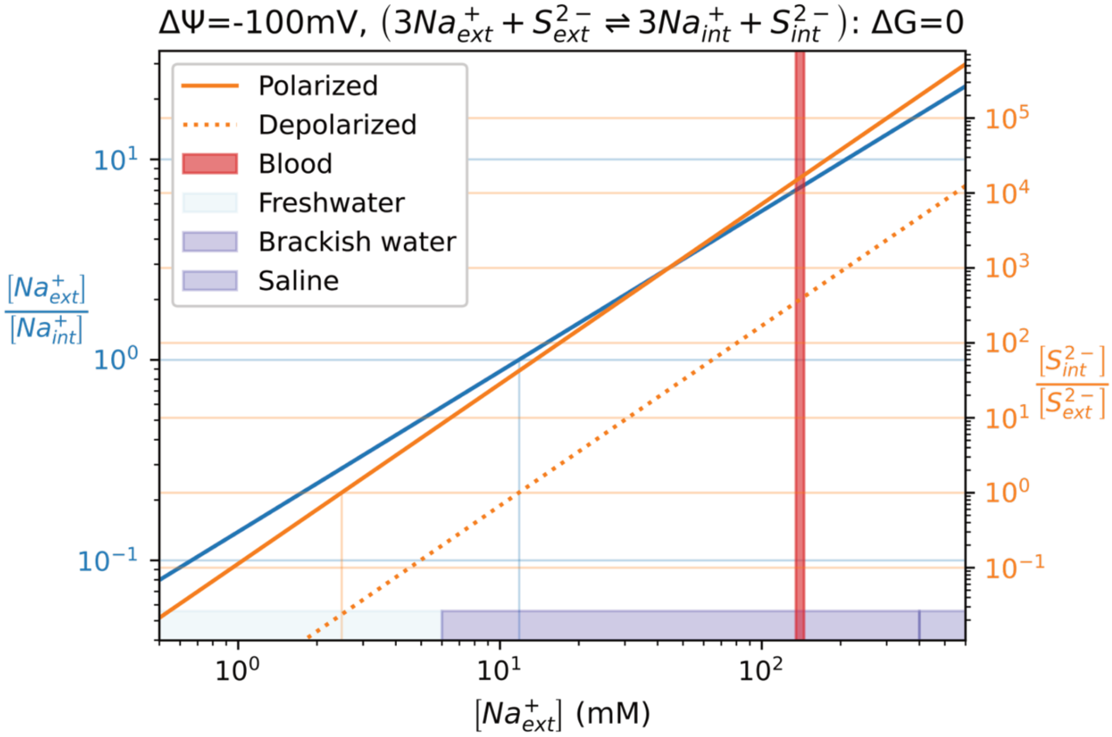

Fig. S12. Estimated physiological Na^+ and succinate concentrations in a bacterial cell in different environments. External (ext) and internal (int) Na^+ concentrations were measured for another gammaproteobacteria, *E. coli*, at pH=7 (23). For *E. coli* at pH=7, the membrane potential difference ($\Delta\psi$) is approximately -100 mV (24). With these numbers, balancing the chemical potential difference and effects of charge for the VcINDY transport reaction at equilibrium provides the internal to external ratio of succinate concentrations for the cell (orange). When $\Delta\psi = 0$, the cell is depolarized (dashed).

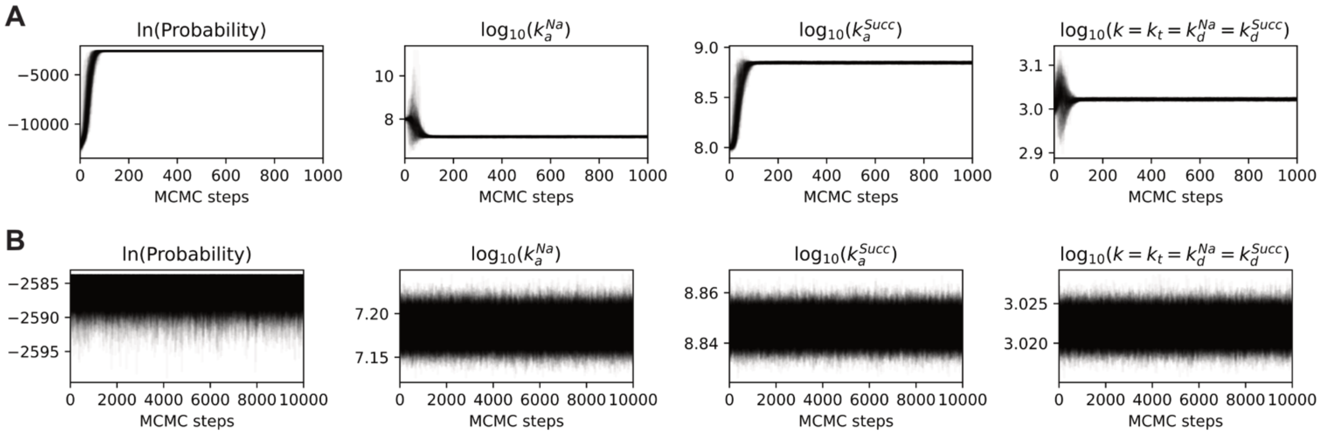

Fig. S13. MCMC trajectories for optimal kinetic model parameters of VcINDY proteoliposome-based succinate transport assay. (A) Affine invariant ensemble MCMC sampler trajectories for 200 walkers during burn-in period. These samples were discarded. (B) Production period trajectories from 200 walkers. Only every 100th sample of those shown here was used to minimize autocorrelation.

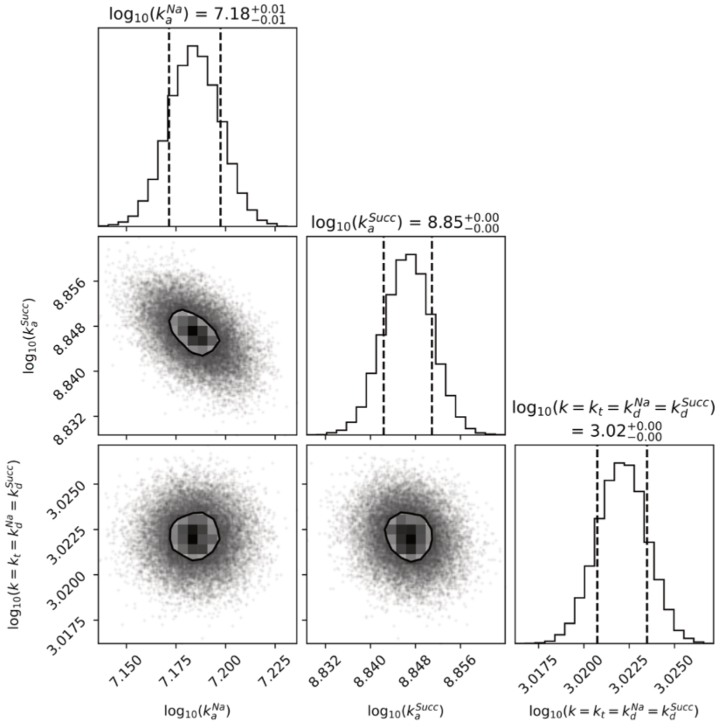

Fig. S14. Corner plot of MCMC samples for optimal kinetic model parameters of VcINDY proteoliposome-based succinate transport assay. Ranges given are the 1σ level containing 39.3% of the sample volume.

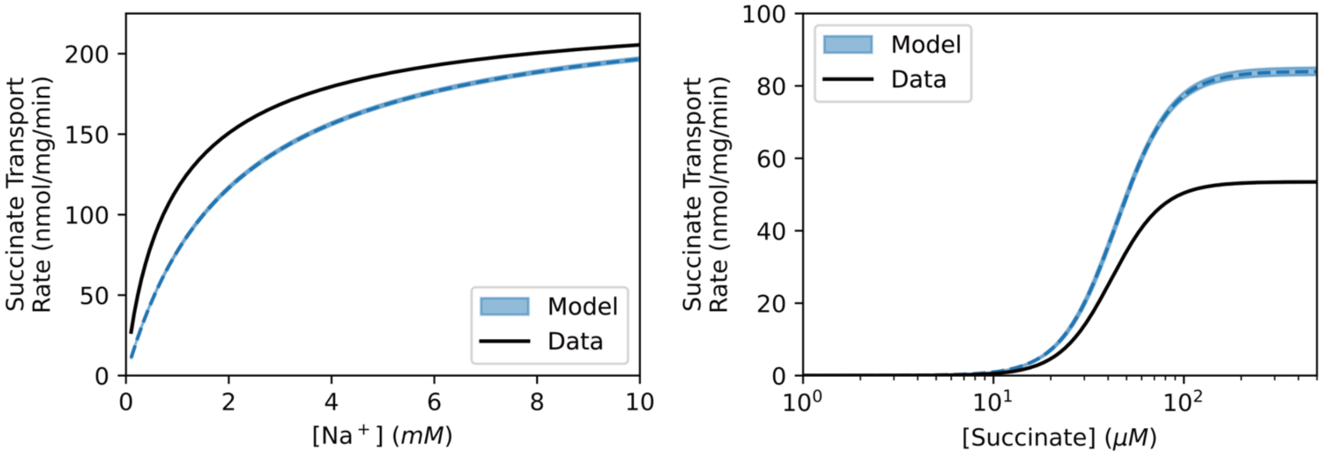

Fig. S15. Modeled VcINDY transport rate experiments. Data from Mulligan and coworkers were reproduced from their reported K_M, V_{max}, and Hill coefficients (10). Modeled data are the 95% credible intervals generated from MCMC samples of k'_a, k''_a, and $\langle k \rangle$, and dashed lines are the lowest energy solution.

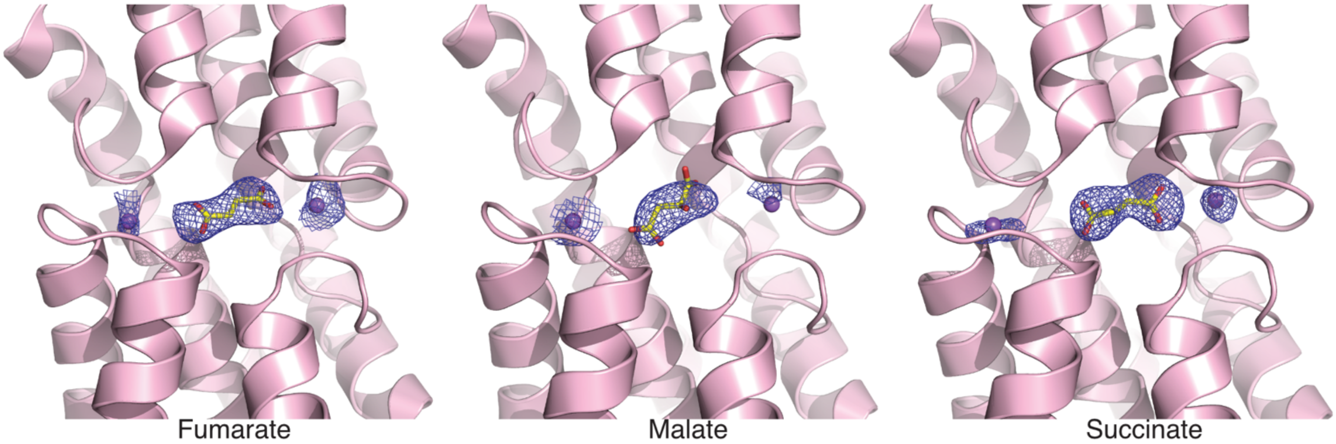

Fig. S16. Structures of the VcINDY binding pocket viewed from the cytosol. The X-ray crystallography derived structures (pink) were determined in the presence of fumarate, malate and succinate, respectively. The electron densities for the sodium and the dicarboxylate substrates are depicted in blue mesh. Sodium ions are shown in purple, and specified dicarboxylate substrates in yellow (carbon) and red (oxygen).

Table S1. E_{FRET} trajectory simulation parameters

Parameter	Value	Units
μ_1	0.1	A.U.
μ_2	0.3	A.U.
μ_3	0.7	A.U.
μ_4	0.9	A.U.
k_{12}	0.25	sec^{-1}
k_{13}	0.50	sec^{-1}
k_{14}	1.00	sec^{-1}
k_{21}	0.50	sec^{-1}
k_{23}	1.00	sec^{-1}
k_{24}	0.25	sec^{-1}
k_{31}	1.00	sec^{-1}
k_{32}	0.25	sec^{-1}
k_{34}	0.50	sec^{-1}
k_{41}	0.25	sec^{-1}
k_{42}	0.50	sec^{-1}
k_{43}	1.00	sec^{-1}
σ	0.20	A.U.
τ	0.01	sec
n	2000	frames
N	400	trajectories

μ is an emission mean, k is a rate constant, σ is a standard deviation of additive noise, τ Is the time period of each data point, n is the length of each trajectory, N is the number of trajectories

Table S2. X-ray crystallography of VcINDY in complex with substrate

	Parameter	VcINDY-succinate	VcINDY-fumarate	VcINDY-malate
Data collection	Wavelength (Å)	0.9791	0.9794	0.9794
	Resolution range (Å)	50.0-3.09 (3.15-3.09)	50-3.29 (3.35-3.29)	50.0-3.50 (3.56-3.50)
	Space group	$P2_1$	$P2_1$	$P2_1$
	Cell dimensions: a, b, c (Å)	105.5, 102.5, 171.1	105.8, 102.1, 171.2	106.8, 102.4, 171.8
	Cell angle: β (°)	98.808	98.937	97.791
	Total reflections	128,621 (6,360)	99,521 (3,598)	86,871 (4,328)
	Unique reflections	65,778 (3,229)	51,510 (1,913)	44,866 (2,248)
	Multiplicity	5.0 (5.1)	6.6 (5.3)	6.9 (6.4)
	Completeness (%)	99.9 (100)	93.9 (71.0)	96.4 (96.9)
	$I/\sigma(I)$	10.3 (0.625)	10.1 (0.667)	10.8 (0.571)
	Wilson B (Å^2)	80.97	110.64	134.20
	R_{pim}	8.4 (152)	4.4 (54.2)	3.5 (61.5)
	$CC_{1/2}$	0.998 (0.443)	0.102 (0.512)	0.997 (0.604)
Refinement	R_{work}/R_{free} (%)	25.3% / 29.6%	24.9% / 28.5%	26.1% / 30.5%
	No. atoms - Protein/Ligands	13,325 / 40	13,097 / 23	12,792 / 42
	RMSD bond lengths (Å)	0.003	0.003	0.001
	RMSD bond angles (°)	0.66	0.52	0.39
	Ramachandran favored (%)	88.7	91.3	93.2
	Ramachandran allowed (%)	9.99	7.30	5.72
	Ramachandran outliers (%)	1.35	1.44	1.12
	Rotamer outliers (%)	0.07	0.0	0.0
	Clashscore	34.26	29.10	23.49

Numbers in parentheses are statistics for the highest resolution shell.

SI References

1. A. R. Verma, K. K. Ray, M. Bodick, C. D. Kinz-Thompson, R. L. Gonzalez, Increasing the accuracy of single-molecule data analysis using tMAVEN. *Biophysical Journal* **123**, 2765–2780 (2024).

2. J. E. Bronson, J. Fei, J. M. Hofman, R. L. Gonzalez, C. H. Wiggins, Learning rates and states from biophysical time series: a Bayesian approach to model selection and single-molecule FRET data. *Biophysical Journal* **97**, 3196–205 (2009).

3. C. D. Kinz-Thompson, K. K. Ray, R. L. Gonzalez, Bayesian Inference: The Comprehensive Approach to Analyzing Single-Molecule Experiments. *Annu. Rev. Biophys.* **50**, 191–208 (2021).

4. J.-W. van de Meent, J. E. Bronson, C. H. Wiggins, R. L. Gonzalez, Empirical Bayes Methods Enable Advanced Population-Level Analyses of Single-Molecule FRET Experiments. *Biophysical Journal* **106**, 1327–1337 (2014).

5. J. Hon, R. L. Gonzalez, Bayesian-Estimated Hierarchical HMMs Enable Robust Analysis of Single-Molecule Kinetic Heterogeneity. *Biophysical Journal* **116**, 1790–1802 (2019).

6. B. J. Berne, R. Pecora, *Dynamic Light Scattering: With Applications to Chemistry, Biology, and Physics*, Unabridged edition (Dover Publications, 2000).

7. K. P. Murphy, “Conjugate Bayesian analysis of the Gaussian distribution” (University of British Columbia, 2007).

8. D. T. Gillespie, A general method for numerically simulating the stochastic time evolution of coupled chemical reactions. *Journal of Computational Physics* **22**, 403–434 (1976).

9. K. K. Ray, A. R. Verma, R. L. Gonzalez, C. D. Kinz-Thompson, Inferring the shape of data: a probabilistic framework for analysing experiments in the natural sciences. *Proc. R. Soc. A.* **478**, 20220177 (2022).

10. C. Mulligan, G. A. Fitzgerald, D.-N. Wang, J. A. Mindell, Functional characterization of a Na$^+$-dependent dicarboxylate transporter from Vibrio cholerae. *Journal of General Physiology* **143**, 745–759 (2014).

11. D. Foreman-Mackey, D. W. Hogg, D. Lang, J. Goodman, emcee: The MCMC Hammer. *Publications of the Astronomical Society of the Pacific* **125**, 306–312 (2013).

12. Z. Otwinowski, W. Minor, Processing of X-ray diffraction data collected in oscillation mode. *Meth. Enzymol.* **276**, 307–326 (1997).

13. R. Nie, S. Stark, J. Symersky, R. S. Kaplan, M. Lu, Structure and function of the divalent anion/Na+ symporter from Vibrio cholerae and a humanized variant. *Nature Communications* **8**, 15009 (2017).

14. P. Emsley, K. Cowtan, Coot: model-building tools for molecular graphics. *Acta Crystallogr D Biol Crystallogr* **60**, 2126–2132 (2004).

15. P. D. Adams, *et al.*, PHENIX: a comprehensive Python-based system for macromolecular structure solution. *Acta Crystallogr D Biol Crystallogr* **66**, 213–221 (2010).

16. R. H. Austin, K. W. Beeson, L. Eisenstein, H. Frauenfelder, I. C. Gunsalus, Dynamics of ligand binding to myoglobin. *Biochemistry* **14**, 5355–5373 (1975).

17. C. D. Kinz-Thompson, N. A. Bailey, R. L. Gonzalez, Precisely and Accurately Inferring Single-Molecule Rate Constants. *Methods Enzymol* **581**, 187–225 (2016).

18. D. A. McQuarrie, Kinetics of Small Systems. I. *The Journal of Chemical Physics* **38**, 433–436 (1963).

19. L. P. Watkins, H. Yang, Detection of Intensity Change Points in Time-Resolved Single-Molecule Measurements. *J. Phys. Chem. B* **109**, 617–628 (2005).

20. B. Shuang, *et al.*, Fast Step Transition and State Identification (STaSI) for Discrete Single-Molecule Data Analysis. *J. Phys. Chem. Lett.* **5**, 3157–3161 (2014).

21. C. D. Kinz-Thompson, R. L. Gonzalez, Increasing the Time Resolution of Single-Molecule Experiments with Bayesian Inference. *Biophysical Journal* **114**, 289–300 (2018).

22. G. Haran, Noise reduction in single-molecule fluorescence trajectories of folding proteins. *Chemical Physics* **307**, 137–145 (2004).

23. C.-J. Lo, M. C. Leake, R. M. Berry, Fluorescence Measurement of Intracellular Sodium Concentration in Single Escherichia coli Cells. *Biophysical Journal* **90**, 357–365 (2006).

24. H. Felle, J. S. Porter, C. L. Slayman, H. R. Kaback, Quantitative measurements of membrane potential in Escherichia coli. *Biochemistry* **19**, 3585–3590 (1980).